ACS OMEGA

Article

http://pubs.acs.org/journal/acsodf

Transport Properties of Hydrogenated Cubic Boron Nitride Nanofilms with Gold Electrodes from Density Functional Theory

Elizane E. de Moraes,[†] Maurício D. Coutinho-Filho,[†] and Ronaldo J. C. Batista*[,‡]

[†]Laboratório de Física Teórica e Computacional, Departamento de Física, Universidade Federal de Pernambuco, Cidade Universitária, 50670-901 Recife, Pernambuco, Brazil

[‡]Departamento de Física, Universidade Federal de Ouro Preto, Campus Morro do Cruzeiro s/n, 35400-000 Ouro Preto, Minas Gerais, Brazil

ABSTRACT: The electrical transport properties of a four-layered hydrogen-terminated cubic boron nitride sub-nanometer film in contact with gold electrodes are investigated via density functional calculations. The sample exhibits *asymmetric metallic* surfaces, a fundamental feature that triggers the system to behave like a typical p−n junction diode for voltage bias in the interval $-0.2 \leq V \leq 0.2$, where a rectification ratio up to 62 is verified. Further, in the wider region $-0.3 \leq V \leq 0.3$, negative differential resistance with a peak-to-valley ratio of 10 is observed. The qualitative behavior of the $I-V$ characteristics is described in terms of the hydrogenated cBN film equilibrium electronic structure. Such a film shows metallic surfaces due to surface electronic states at a fraction of eV above and below the Fermi level of the N−H terminated and B−H terminated surfaces, respectively, with a wide bulk-band gap characteristic of BN materials. Such a mechanism is supported by transmission coefficient calculations, with the Landauer−Büttiker formula governing the $I-V$ characteristics.

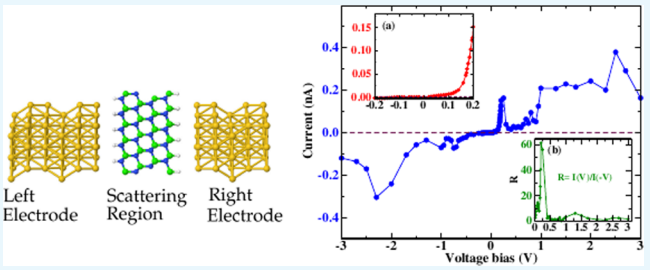

1. INTRODUCTION

Boron and nitrogen can be combined to form a binary compound, boron nitride (BN), which exists in the same crystalline forms as the respective carbon allotropes. In three dimensions, cubic BN (cBN) and wurtzite BN are the analogs of diamond and lonsdaleite, respectively.[1,2] In two dimensions, the analog of graphene is hexagonal BN (hBN)[3−8] or white graphene and, in one dimension, BN can also form nanoribbons[9,10] and nanotubes.[11,12] As boron and nitrogen are the left and right neighbors of carbon in the periodic table, respectively, similarly structured carbon and BN materials show similar isoelectronic bonds. However, unlike the C−C bond, the B−N bond is polar, which may lead to distinct electronic and optical properties of BN structures in comparison to those of their carbon analogs. For instance, although graphene is a semimetal, hBN presents a wide band gap, about 5−6 eV.[3−6,8] Therefore, BN nanotubes, which can be seen as an hBN layer wrapped into a cylinder, are always wide-band gap semiconductors whereas carbon nanotubes can be either metallic or semiconducting. In addition, because BN is a binary compound the surfaces and edges of BN materials, unlike those of carbon materials, can be either boron or nitrogen terminated. Thus, BN and carbon materials, whose bulk properties are alike, such as cBN and diamond, can present distinct electrochemical properties due to differences in surface termination. Besides, in situations where the surface/bulk ratio is large, such as the case of thin cBN films and narrow nanoribbons, the surface termination can change the properties of the system as a whole.[13,14] Very recently, a detailed study of the growth process of 2D hBN was reported,[15] in which case large single-crystal monolayer domains with controlled morphology and straight merging boundaries were identified. The merging boundaries were revealed by optical microscopy upon hydrogen etching at elevated temperatures, thereby providing the possibility to fabricate hBN ribbons by etching parallel grain boundaries.

Because clean diamond and cBN surfaces are usually unstable, reconstructions and/or adsorption of environmental chemical species are often observed.[16] Reconstructions and covalent functionalization of the (111) surface by several chemical species have already been investigated by means of first-principles techniques, which have indicated that H and F atoms are efficient as stabilizing agents.[17] Such predictions have been verified experimentally, where fluorination of hBN−graphene−hBN multilayers might result in hybrid cBN/diamond nanofilms with sp^3 hybridization throughout the structures.[18] In addition, fluorination of few-layered hBN sheets can lead to formation of thermodynamically favorable F-terminated cBN nanofilms with an embedded N−N bond layer.[19] It has also been demonstrated that such covalent functionalization has a strong effect on BN electron transport properties.[20,21] For the hBN analog, graphene, hydrogenation is a reversible process in which sp^2 bonds can be converted into sp^3 bonds and vice-versa.[22] In addition, it is possible to produce functionalized diamond films (111) oriented from few-layered

Received: January 18, 2017
Accepted: April 18, 2017
Published: April 27, 2017

DOI: 10.1021/acsomega.7b00061
ACS Omega 2017, 2, 1696−1701

graphene by applying pressure with an AFT tip.[23] In principle, such a process can be used to produce cBN films very similar to that employed in this work. In particular, a gold AFM tip could generate a metal−film interface analogous to that of our model, whereby a thin (111) oriented hydrogenated cBN film is placed between gold contacts, as is detailed in the next section.

The C−H, B−H, and N−H bonds are not isoelectronic; therefore, H-terminated diamond and H-terminated cBN must present distinct electrochemical properties. Recent theoretical works indicate that B−H and N−H terminated cBN surfaces are *metallic*,[13,14] which is surprising because BN materials are known for being wide gap insulators. The same works have also shown that the band gap of thin H-terminated cBN films depends on the film thickness, because, in a very thin film, opposite B−H and N−H terminated surfaces interact with each other.[13,14] A H-terminated cBN film was found to become metallic when its thickness exceeded a critical threshold of 0.72 nm.[13,14] However, the band gap of thin diamond films is nearly constant no matter the film thickness.[4,13]

Unlike thin diamond films, nanofilms of cBN have *asymmetrical* surfaces: one N-terminated and one B-terminated surface. Such asymmetric cBN films are expected to present interesting rectifying effects, which is indeed supported by experimental and theoretical reports.[9,12,24−28] Among them, it is worth mentioning the experimental study[28] where clear rectification in cBN/sp^2BN/Si heterojunctions is observed. Further, the electron transport behavior is characteristic of typical p−n junction diodes over a range of temperatures varying from 298 up to 573 K. Very recently, another study on the thermal stability of BN/Si p−n heterojunction diodes was also reported.[29] Such results are interesting and present technological appeal because the cBN films can be less than 1 nm thick (for the sake of comparison, the depletion width of a p−n diode is over 50 nm wide[30]), which may allow for further miniaturization of optoelectronic devices. Most importantly, new light-emitting diode properties were verified on heterostructures of stacked 2D materials formed by hBN, graphene, and MoS_2, weakly coupled by van der Waals forces.[31] We would like to emphasize that many BN nanostructure properties have been recently reviewed, including their fabrication, functionalization, and applications.[32] In addition, the use of Au nanofilms and nanoparticles in the presence of BN films has attracted the attention of researchers with a focus on industrial applications,[33] including very interesting electrochemical properties.[34]

In this work, we employ first-principles calculations based on density functional theory (DFT) and nonequilibrium Green's function formalism to explore the electron transport properties of very thin hydrogenated BN films coupled to metallic gold electrodes. This work is organized as follows. Methodology and computational details are given in Section 2, and the results and discussion are presented in Section 3. Section 4 ends the text with our concluding remarks.

2. METHODOLOGY AND COMPUTATIONAL DETAILS

Our electronic structure calculations were performed within the framework of DFT,[35,36] as implemented in the SIESTA program.[37] We used Troullier−Martin norm conserving relativistic pseudopotentials in Kleinman−Bylander nonlocal form.[38,39] The exchange and correlation energies were treated within the generalized gradient approximation according to the Perdew, Burke, and Ernzerhof (PBE) parametrization.[40,41] The Khon−Sham eigenfunctions were expanded in a linear combination of numerical atomic orbitals[42] of finite range. The range of the orbitals was determined by the common energy shift (0.01 Ry) in the energy eigenvalues imposed by confining potentials in the pseudoatom problem. The split valence and perturbative polarization methods were employed to generate a double-zeta basis for each angular momentum plus polarization orbitals (the standard SIESTA DZP basis set). The Brillouin zone was sampled using a 1 × 1 × 30 Monkhorst−Pack grid and a minimal 150 Ry mesh-cutoff energy was used to determine real space grid fineness. Nonequilibrium Green's function techniques[43,44] within the DFT framework previously described (which is implemented in the TRANSIESTA program[43]) were employed to address the electron transport properties. The current through the scattering region was calculated using the Landauer−Büttiker formula[45,46]

$$I(V) = \frac{2e^2}{h}\int_{-\infty}^{\infty}\{T(E, V)[f_L(E-\mu_L) - f_R(E-\mu_R)]\}\,dE \quad (1)$$

where e is the electron charge, h is Planck's constant, $T(E, V)$ is the transmission probability of electrons incident at energy E from the left to the right electrode under an applied voltage bias V, $f_{L(R)}$ is the Fermi−Dirac distribution function for the left (right) electrode with the respective chemical potential $\mu_L = E + \frac{V}{2}$ (and $\mu_R = E - \frac{V}{2}$) shifted upwards (downwards) relative to the Fermi energy E_F. More specifically[43,44]

$$T(E, V) = \mathrm{Tr}[\mathrm{Im}\sum_L(E)G^{\dagger}(E)\mathrm{Im}\sum_R(E)G(E)] \quad (2)$$

where $\sum_L(E)$ [$\sum_L(R)$] is the self-energy of the left (right) electrode, $G(E)$ is the solution of the equation $(E - H)^{-1} = G(E)$, in a matrix format, with H including the Hamiltonians of the sample (scattering region) and electrodes with their respective self energies, and the off-diagonal terms related to the interaction between these elements (contact region). The nonequilibrium solution is obtained in a DFT self-consistent fashion,[43] with the Landauer−Büttiker formula governing the $I-V$ characteristics.

Our model is divided into three regions: left and right semi-infinite electrodes oriented in the (111) direction, and the scattering region. The scattering region, indicated in Figure 1, contains the hydrogenated cBN film and part of the left and

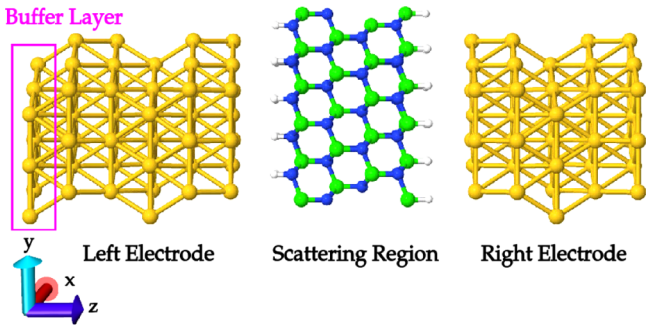

Figure 1. Hydrogenated cBN nanofilm is composed of a four-layered cBN film oriented in the (111) direction and passivated with hydrogen at the two opposite surfaces, wherein the H atoms bind to the N atoms (B atoms), thus forming the N−H (B−H) terminated surface. The scattering region contains the hydrogenated cBN film and part of the left and right gold electrodes. Au atoms are yellow, B atoms are green, N atoms are blue, and H atoms are white.

DOI: 10.1021/acsomega.7b00061
ACS Omega 2017, 2, 1696−1701

right gold electrodes, which are connected to the left and right semi-infinite electrodes in the transport calculations. Figure 2a,b shows the front and side views of the Au(111) oriented

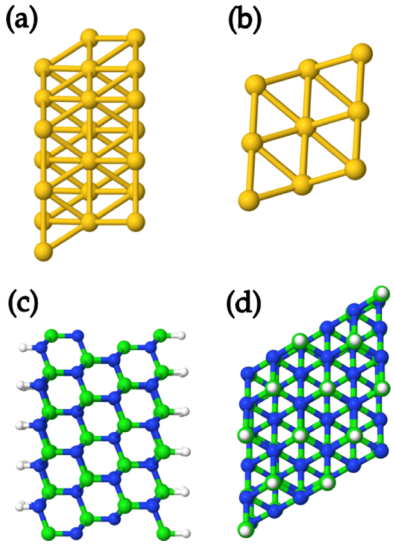

Figure 2. Top panels: (a) front and (b) side views of the Au(111) oriented right electrode. Lower panels: (c) front and (d) side view of the hydrogenated four-layered cBN film.

right electrode, respectively, used to calculate the right self-energy. It is composed of three Au(111) oriented layers, and each layer contains nine Au atoms. The left Au electrode used to calculate the left self-energy is the mirror image of the right electrode shown in Figure 2a,b.

The hydrogenated cBN film shown in Figure 2c,d is composed of a four-layered cBN(111)-oriented film passivated with hydrogen at the surfaces, wherein the H atoms bind to the N atoms to the left (B atoms to the right), thus forming the N−H terminated surface (B−H terminated surface). The layers of the hydrogenated cBN film are bound together more tightly than those of the bulk cBN;[13] the bond length of the B−N bonds that connect the BN layers of the film is shorter (1.5 Å[13]) than that of the B−N bonds in bulk cBN (1.56 Å[13,47]). However, the B−N bonds of the same layer are longer (1.60 Å[13]) than the bulk B−N bonds. The scattering region also contains part of the electrodes (10 Au layers) to ensure a smooth connection of the hydrogenated cBN film to the semi-infinite electrodes. In addition, it can be seen in Figure 1 that the left side of the scattering region contains one extra layer of Au atoms (buffer atoms); such a layer was added to allow the match between successive periodic images in calculations where periodic boundary conditions are imposed. In transport calculations, with open boundary conditions, such a buffer layer is not taken into account and the electrode connects to the following Au layer, whose geometry was chosen to match that of the right layer of the left electrode. In total, Figure 1 is composed of 99 Au, 24 H, 48 B, and 48 N atoms.

The geometry shown in Figure 1 was optimized using the conjugated gradient algorithm, where the lattice is relaxed together with the atomic coordinates. The cell parameters and atomic positions were optimized until both the maximum component of the stress tensor and the force on atoms were smaller than 1.0 GPa and 0.05 eV/Å, respectively. The obtained unit cell vectors are $a\left(\frac{\sqrt{3}\hat{i}}{2}, \frac{\hat{j}}{2}\right)$, $a\hat{j}$, and $4.25a\hat{k}$, where a = 8.94 Å. The obtained values of the B−N bonds were 1.52 Å (for B−N bonds that connect any of the film layers) and 1.58 Å (for any bond in the same layer), which indicates that contact with gold does not have a strong affect on film geometry. The average value obtained for the Au−Au bond (2.96 Å) is similar to that obtained using similar DFT−PBE approaches (2.97 Å).[48] The Au−Au bonds in the same (111) plane are stretched due to the imposed commensurability with the cBN film; however, the increase (0.03 Å or 1%) is small and it is reasonable to argue that the hydrogenated cBN film and the Au layers commensurate within the calculation precision. Also, the distance between neighbor Au planes is constant (2.35 Å), which suggests that the effect of the interaction with the film surface on the Au layer geometry is negligible. The N−H and B−H distances are, respectively, 1.03 and 1.21 Å. We also found two different equilibrium distances between gold and the hydrogenated cBN film: 2.6 and 2.8 Å for the Au/N−H and Au/B−H interfaces, respectively. Such a result indicates that interaction between gold and the N−H surface is stronger than that with the B−H surface. A rough estimative of the magnitude of the interaction between the hydrogenated cBN film and the gold slabs can be obtained by increasing the H−Au distances of both interfaces. For distance values of H−Au of 3, 4, and 5 Å, our calculated free energies (relative to the equilibrium total energy) are 9.2, 13.5, and 16.6 eV, respectively. Such values suggest a binding energy per unit of area greater than 0.3 eV/Å^2, which is an interaction stronger than typical dispersive van der Waals interactions (for the sake of comparison, the binding energy per unit of area between graphene layers is about 0.01 eV/Å^2).[49] Such a result is expected because the hydrogenated cBN film presents charged surfaces that should induce surface charge on gold surfaces.

3. RESULTS AND DISCUSSION

Figure 3 shows the current−voltage $I-V$ characteristics of the system described in Figure 1 for the bias range varying from −3.0 to 3.0 V. A positive bias V is obtained by shifting the Fermi levels of the left and right electrodes by $\frac{eV}{2}$ and $-\frac{eV}{2}$,

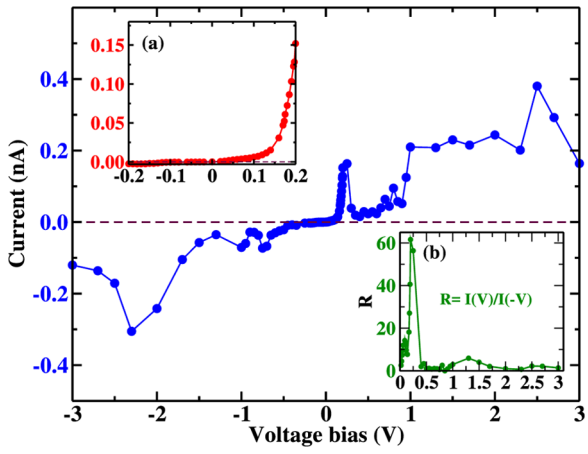

Figure 3. $I-V$ characteristics of the system shown in Figure 1 for the bias range $-3.0 \le V \le 3.0$ V. Inset (a) displays a zoom of the interval $-0.2 \le V \le 0.2$, thus unveiling a behavior very similar to that observed in p−n junction diodes. Inset (b) exhibits the rectification ratio $R = \frac{I(V)}{|I(-V)|}$, whose salient feature is the big peak of 62 at 0.2 V, thus confirming the diode behavior and the observed negative differential resistance.

DOI: 10.1021/acsomega.7b00061
ACS Omega 2017, 2, 1696−1701

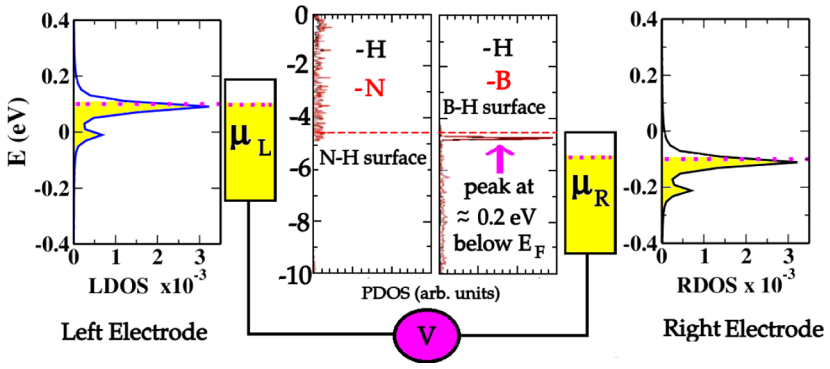

Figure 4. Scheme illustrating the system shown in Figure 1 under a voltage bias of $V = 0.2$ V. The left (right) panel shows the PDOS on the surface of the left (right) electrode in the energy interval $-0.4 \leq E \leq 0.4$ eV. The central panel exhibits the PDOS on the N−H (B−H) surface in the wider energy interval: $-10 \leq E \leq 0$ eV (the dashed line indicates the Fermi level, which, to comply with the energy scale of the electrodes, must be set at $E_F \equiv 0$). Under the bias, the chemical potential μ_L of the left (right) electrode is shifted upwards (downwards) by 0.1 (−0.1) eV relative to the Fermi level. Notice the sharp peak ≈0.2 eV below the Fermi level on the B−H surface. As explained in the text, electrons can flow from left to right electrode due to the peculiar combination of the PDOS shown in the above scheme.

respectively. Thus, a positive current flows from the left to the right electrode, and a negative current flows in the opposite direction. It can be seen in Figure 3 that the calculated $I-V$ characteristics sharply differ from that expected for a symmetric scattering region, that is, $-I(-V) \neq I(V)$. In particular, in the voltage range between −0.2 and 0.2 V, as shown in the inset of Figure 3, the absolute values of current obtained for a positive bias are much larger than that obtained for a negative bias, which is the typical $I-V$ curve observed for p−n junction diodes. Such a behavior can be better seen in a plot of the rectification ratio $\left(R = \frac{I(V)}{|I(-V)|}\right)$ as a function of the voltage, as can been seen in the inset B of Figure 3. The maximum rectification occurs for values of V of about 0.2 V, where the rectification ratio is about 62.

Outside the voltage range between −0.2 and 0.2 V, the $I-V$ curve of the thin hydrogenated cBN film sharply differs from that of an ordinary p−n junction diode. Just above 0.2 V, a region of negative differential resistance (NDR, i.e., increased resistance with increasing voltage) with a peak-to-valley ratio of about 10 is observed, which could be useful in practical applications, such as NDR devices. For the sake of comparison, the peak-to-valley ratio of organic thiolated molecules is about 1.6.[50] Such a fast drop in current with increased voltage leads to a fast decrease in the rectification ratio, as can be seen in the inset B of Figure 3, which would limit the use of hydrogenated cBN thin films as rectifiers to the range between −0.2 and 0.2 V.

To understand the origin of the asymmetric behavior of the $I-V$ curve, we further investigated the electronic structure of the hydrogenated four-layered cBN film. The density of electron states projected (PDOS) on the H and N atoms of the N−H terminated surface and on the B and H atoms of the B−H terminated surface is shown in the middle panels of Figure 4. It can be seen that the N−H terminated surface is metallic but it presents, just below the Fermi level, a wide energy gap (over 4 eV wide), where there are no electron levels available. On the other hand, the density of electron states projected on the H and B atoms of the B−H surface shows a wide energy gap (also over 4 eV wide) just above the Fermi level. In addition, a sharp peak in the density of electron states for the B−H surface is observed just below the Fermi level, which shows the existence of an electron state localized near the B−H bond. We stress that the PDOS on the N−H and B−H surfaces displayed in the central panel of Figure 4 is consistent with the calculated electronic band structure of hydrogenated cBN.[13,14] Both the B−H and N−H terminated surfaces are metallic. However, in the case of the N−H terminated surface, the Fermi levels are near the bottom of bands with positive curvature above a wide band gap. Meanwhile, at the B−H terminated surface, the Fermi level is near the top of bands with negative curvature just below an energy gap.[13,14] As demonstrated by Zhang and Guo,[13] the electron states near the Fermi level in the N−H terminated surfaces are due to p_z orbitals of N atoms binding H atoms (where the z direction is perpendicular to the film). Those states are peaked outside the nanofilm (at 2.2 Å from the N-end surface) and behave like nearly free electron states. On the other hand, the electron levels near the Fermi level at the B−H terminated surface are due to p_x and p_y orbitals of N atoms near to the B−H terminated surface.[13] This can be understood in terms of the polar nature of B−N sp^3 bonds, which are isoelectronic to the apolar sp^3 C−C bonds. In the cBN bulk, the excess of electrons of the N orbitals is precisely offset by the lack of electrons in the B orbitals (as a result, cBN presents a band gap as wide as that of diamond carbon). In the case of the N−H terminated surface, the N atoms cannot transfer electrons to the H atoms as they do to the B atoms, which results in the semioccupied p_z bands mentioned before. Likewise, the B atoms of the B−H terminated surface cannot receive electrons from H atoms as they do from the N atoms, which affects the sp^3 B−N bonds just below the B−H terminated surface, giving rise to the semioccupied p_x and p_y orbitals and the observed peak in the PDOS on the referred surface.

On the basis of the discussed electronic structure of the hydrogenated cBN film, we propose a mechanism that describes the qualitative behavior of the $I-V$ curve shown in Figure 3a for a small applied bias, as illustrated in Figure 4. The left and right panels of that figure show the projected density of states on the left (LDOS) and right (RDOS) electrodes, respectively, when a voltage bias of $V = 0.2$ V is applied to the system, see Figure 4c. The chemical potential μ_L of the left electrode (magenta dotted line) is shifted 0.1 eV upwards in comparison with its original equilibrium position (red dashed line), and the chemical potential μ_R of the right electrode is shifted 0.1 eV downwards. Because there are empty levels

DOI: 10.1021/acsomega.7b00061
ACS Omega 2017, 2, 1696−1701

available (below the Fermi surface) on the N−H terminated surface in contact with the left electrode and occupied levels (below the Fermi surface) on the B−H terminated surface in contact with the right electrode, electrons can flow from left to right electrode. On the other hand, when a negative bias of $V = -0.2$ V is applied, the new configuration of Figure 4 is equivalent to an exchange of LDOS with RDOS, as shown in Figure 5b,c, and the current traveling from right to left

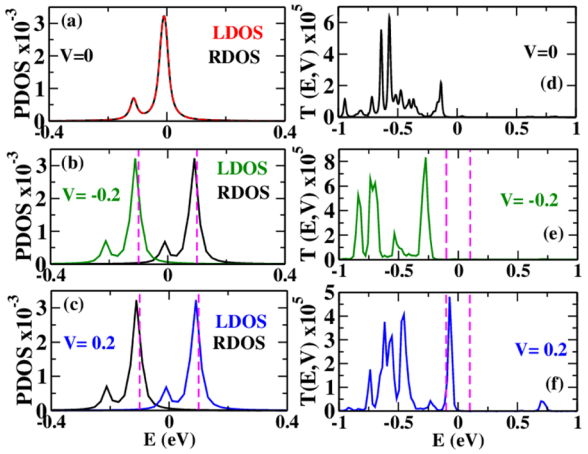

Figure 5. PDOS at the surface atoms of the left (LDOS) and right (RDOS) electrodes are shown in (a), (b), and (c) at the voltages bias $V = 0$, −0.2, and 0.2 V, respectively. The LDOS and RDOS in (c) are those used in Figure 4. Transmission coefficients of the system shown in Figure 1 are displayed in (d), (e), and (f) for the corresponding voltages used in (a), (b), and (c), respectively. For $V = -0.2$ V, the current is null as $T(E)$ is practically zero in the interval $-0.1 \leq V \leq 0.1$, whereas for $V = 0.2$ V, a peak confirms the mechanism illustrated in Figure 4 and the diode behavior shown in the inset (a) of Figure 3.

electrode is strongly blocked by Coulomb repulsion. In short, when a small positive bias is applied, the current traveling from right to left electrode is very small in comparison to that traveling from left to right electrode. However, a large voltage bias strongly affects the electronic structure of the hydrogenated four-layered cBN film, and therefore the mechanism described in Figure 4 is not expected to hold in such a situation.

The mechanism discussed above assumes that the transmission coefficient used to obtain the current is proportional to the hydrogenated four-layered cBN equilibrium density of states for small values of applied bias. Because there are energy gaps in the occupied states on the N−H terminated surface and the empty states on the N−H terminated surface, it is expected that the transmission coefficients within the Landauer−Büttiker formula under the integration window would be roughly zero for small values of negative applied bias. Indeed, it can be seen in Figure 5e that the transmission coefficient between −0.1 and 0.1 eV is approximately null when a bias of $V = -0.2$ V is applied. However, Figure 5f shows a peak in the transmission coefficient within the integration window for a bias of $V = 0.2$ V, which is also expected based on the existence of a peak in the PDOS on the B−H surface, as shown in the central panel of Figure 4. Because the hydrogenated cBN film is metallic, the band gap problem should not prevent PBE calculations from correctly predicting the Fermi level alignment relative to the gold electrode. In any case, we also argue that if a more elaborate calculation indicates a small change in the location of the sharp peak in the density of states for the B−H surface, the peak in $T(E, V)$ and the corresponding p−n junction diode behavior, shown in Figures 5f and 3a, respectively, would both sustain if the voltage bias is tuned accordingly, so as to allow the referred sharp peak to contribute to the current. Lastly, we remark that in our work, about a hundred $T(E, V)$ curves (for voltage bias between −3 and 3) have been calculated to obtain, by means of eq 1, each one of the values of current shown in Figure 3 for a given voltage V. Similarly to the case of $T(E, V = \pm 0.2$ V), shown in Figure 5, the scale of any other calculated $T(E, V)$ curve is of the order 10^{-5}.

4. CONCLUSIONS

We employed the nonequilibrium Green's function formalism within the DFT framework and the Landauer−Büttiker formula to investigate the electron transport properties of a hydrogen-terminated four-layered cBN nanofilm in contact with gold electrodes. This system with asymmetric metallic surfaces gives rise to remarkable transport properties. Indeed, we observed an $I-V$ curve similar to that of a p−n junction diode for values of voltage between −0.2 and 0.2 V, with a rectification ratio up to 62. In addition, just above 0.2 V, a region of negative differential resistance with a peak-to-valley ratio of about 10 is observed. The qualitative behavior of the obtained $I-V$ curve is explained based on features of the hydrogenated cBN nanofilm equilibrium electronic structure, and ab initio calculation of the transmission coefficient. The reported results add relevant information of both intrinsic interest and potential applications in the realm of nanoelectronics.

AUTHOR INFORMATION

Corresponding Author

*E-mail: batista.rjc@gmail.com. Phone: +55(31)3559-1667.

ORCID

Ronaldo J. C. Batista: 0000-0002-7471-4968

Notes

The authors declare no competing financial interest.

ACKNOWLEDGMENTS

We acknowledge the Brazilian science agencies CNPq, FACEPE, FAPEMIG, and CAPES. R.J.C.B. thanks PROPP-UFOP for the Auxílio Financeiro a Pesquisador-Custeio 2016 and CNPq/FAPEMIG through the project INCT de Nanomateriais de Carbono. M.D.C.-F. thanks the CNPq/FACEPE through the PRONEX Program.

REFERENCES

(1) Xu, Y.-N.; Ching, W. Y. *Phys. Rev. B* **1991**, *44*, 7787−7798.

(2) Mirkarimi, P. B.; McCarty, K. F.; Medlin, D. L. *Mater. Sci. Eng., R* **1997**, *21*, 47−100.

(3) Zunger, A.; Katzir, A.; Halperin, A. *Phys. Rev. B* **1976**, *13*, 5560−5573.

(4) Blase, X.; Rubio, A.; Louie, S. G.; Cohen, M. L. *Phys. Rev. B* **1995**, *51*, 6868−6875.

(5) Liu, L.; Feng, Y.; Shen, Z. *Phys. Rev. B* **2003**, *68*, No. 104102.

(6) Arnaud, B.; Lebegue, S.; Rabiller, P.; Alouani, M. *Phys. Rev. Lett.* **2006**, *96*, No. 026402.

(7) Oliveira, C. K.; Gomes, E. F.; Prado, M. C.; Alencar, T. V.; Nascimento, R.; Malard, L. M.; Batista, R. J.; de Oliveira, A. B.; Chacham, H.; de Paula, A. M.; et al. *Nano Res.* **2015**, *8*, 1680−1688.

(8) Cassabois, G.; Valvin, P.; Gil, B. *Nat. Photonics* **2016**, *10*, 262−266.

(9) Shi, X.; Dai, Z.; Zheng, X.; Zeng, Z. *J. Phys. Chem. B* **2006**, *110*, 16902−16907.

DOI: 10.1021/acsomega.7b00061
ACS Omega 2017, 2, 1696−1701

(10) (a) Zhang, Z.; Guo, W. *Phys. Rev. B* **2008**, *77*, No. 075403. (b) Zhang, Z.; Guo, W.; Yakobson, B. I. *Nanoscale* **2013**, *5*, 6381−6387.
(11) Chopra, N. G.; Luyken, R.; Cherrey, K.; Crespi, V. H.; Cohen, M. L.; Louie, S. G.; Zettl, A. *Science* **1995**, *269*, 966−967.
(12) Jiuxu, S.; Yintang, Y.; Hongxia, L.; Lixin, G. *J. Semicond.* **2011**, *32*, No. 042003.
(13) Zhang, Z.; Guo, W. *Nano Lett.* **2012**, *12*, 3650−3655.
(14) Moraes, E. E.; Manhabosco, T. M.; de Oliveira, A. B.; Batista, R. J. C. *J. Phys.: Condens. Matter* **2012**, *24*, No. 475502.
(15) Yin, J.; Yu, J.; Li, X.; Li, J.; Zhou, J.; Zhang, Z.; Guo, W. *Small* **2015**, *11*, 4497−4502.
(16) Reinke, P.; Oelhafen, P.; Feldermann, H.; Ronning, C.; Hofsäss, H. *J. Appl. Phys.* **2000**, *88*, 5597−5604.
(17) Larsson, K.; Carlsson, J.-O. *J. Phys. Chem. B* **1999**, *103*, 6533−6538.
(18) Zhang, Z.; Zeng, X. C.; Guo, W. *J. Phys. Chem. C* **2011**, *115*, 21678−21684.
(19) Zhang, Z.; Zeng, X. C.; Guo, W. *J. Am. Chem. Soc.* **2011**, *133*, 14831−14838.
(20) Du, M.; Li, X.; Wang, A.; Wu, Y.; Hao, X.; Zhao, M. *Angew. Chem., Int. Ed.* **2014**, *126*, 3719−3723.
(21) Xue, Y.; Liu, Q.; He, G.; Xu, K.; Jiang, L.; Hu, X.; Hu, J. *Nanoscale Res. Lett.* **2013**, *8*, No. 49.
(22) Elias, D. C.; Nair, R. R.; Mohiuddin, T.; Morozov, S.; Blake, P.; Halsall, M.; Ferrari, A.; Boukhvalov, D.; Katsnelson, M.; Geim, A.; et al. *Science* **2009**, *323*, 610−613.
(23) Barboza, A. P.; Guimaraes, M. H.; Massote, D. V.; Campos, L. C.; Barbosa Neto, N. M.; Cancado, L. G.; Lacerda, R. G.; Chacham, H.; Mazzoni, M. S.; Neves, B. R. *Adv. Mater.* **2011**, *23*, 3014−3017.
(24) Deng, X. Q.; Zhang, Z. H.; Tang, G. P.; Fan, Z. Q.; Qiu, M.; Guo, C. *Appl. Phys. Lett.* **2012**, *100*, No. 063107.
(25) Mohammad, S. N. *Solid-State Electron.* **2002**, *46*, 203−222.
(26) Yang, Z.-D.; Wu, W.; Zeng, X. C. *J. Mater. Chem. C* **2014**, *2*, 2902−2907.
(27) Fakhrabada, D. V.; Ashhadi, M. *Phys. E* **2012**, *44*, 2105−2109.
(28) Teii, K.; Hori, T.; Mizusako, Y.; Matsumoto, S. *Appl. Mater. Interfaces* **2013**, *5*, 2535−2539.
(29) Teii, K.; Mizusako, Y.; Hori, T.; Matsumoto, S. *J. Appl. Phys.* **2015**, *118*, No. 155102.
(30) Cortes-Mestizo, I. E.; Espinosa-Vega, L. I.; Espinoza-Figueroa, J. A.; Cisneros-de-la Rosa, A.; Eugenio-Lopez, E.; Mendez-Garcia, V. H.; Briones, E.; Briones, J.; Zamora-Peredo, L.; Droopad, R.; et al. *J. Vac. Sci. Technol., B: Nanotechnol. Microelectron.: Mater., Process., Meas., Phenom.* **2016**, *34*, No. 02L110.
(31) Withers, F.; Del Pozo-Zamudio, O.; Mishchenko, A.; Rooney, A.; Gholinia, A.; Watanabe, K.; Taniguchi, T.; Haigh, S.; Geim, A.; Tartakovskii, A.; et al. *Nat. Mater.* **2015**, *14*, 301−306.
(32) Yin, J.; Li, J.; Hang, Y.; Yu, J.; Tai, G.; Li, X.; Zhang, Z.; Guo, W. *Small* **2016**, *12*, 2942−2968.
(33) (a) Bello, I.; Chong, Y.; Leung, K.; Chan, C.; Ma, K.; Zhang, W.; Lee, S.; Layyous, A. *Diamond Relat. Mater.* **2005**, *14*, 1784−1790. (b) Meng, X.; Zhang, W.; Chan, C.; Lee, C.; Bello, I.; Lee, S. *Appl. Phys. Lett.* **2006**, *88*, No. 031904.
(34) (a) Uosaki, K.; Elumalai, G.; Noguchi, H.; Masuda, T.; Lyalin, A.; Nakayama, A.; Taketsugu, T. *J. Am. Chem. Soc.* **2014**, *136*, 6542−6545. (b) Elumalai, G.; Noguchi, H.; Lyalin, A.; Taketsugu, T.; Uosaki, K. *Electrochem. Commun.* **2016**, *66*, 53−57.
(35) Hohenberg, P.; Kohn, W. *Phys. Rev.* **1964**, *136*, B864−B871.
(36) Kohn, W.; Sham, L. J. *Phys. Rev.* **1965**, *140*, A1133−A1138.
(37) Soler, J. M.; Artacho, E.; Gale, J. D.; García, A.; Junquera, J.; Ordejón, P.; Sánchez-Portal, D. *J. Phys.: Condens. Matter* **2002**, *14*, 2745−2779.
(38) Kleinman, L.; Bylander, D. M. *Phys. Rev. Lett.* **1982**, *48*, 1425−1428.
(39) Troullier, N.; Martins, J. L. *Phys. Rev. B* **1991**, *43*, 1993−2006.
(40) Perdew, J. P.; Burke, K.; Ernzerhof, M. *Phys. Rev. Lett.* **1996**, *77*, 3865−3868.
(41) Staroverov, V. N.; Scuseria, G. E.; Perdew, J. P.; Davidson, E. R.; Katriel, J. *Phys. Rev. A* **2006**, *74*, No. 044501.
(42) Sánchez-Portal, D.; Ordejon, P.; Artacho, E.; Soler, J. M. *Int. J. Quantum Chem.* **1997**, *65*, 453−461.
(43) Brandbyge, M.; Mozos, J.-L.; Ordejón, P.; Taylor, J.; Stokbro, K. *Phys. Rev. B* **2002**, *65*, No. 165401.
(44) Mozos, J. L.; Ordejón, P.; Brandbyge, M.; Taylor, J.; Stokbro, K. *Nanotechnology* **2002**, *13*, 346−351.
(45) Büttiker, M.; Imry, Y.; Landauer, R.; Pinhas, S. *Phys. Rev. B* **1985**, *31*, 6207−6215.
(46) Nazarov, Y.; Blanter, Y. *Quantum Transport Introduction to Nanoscience*; Cambridge University Press: New York, 2009.
(47) Batista, R. J. *Chem. Phys. Lett.* **2010**, *488*, 209−212.
(48) Kim, T.; Liu, Z.-F.; Lee, C.; Neaton, J. B.; Venkataraman, L. *Proc. Natl. Acad. Sci. U.S.A.* **2014**, *111*, 10928−10932.
(49) de Lima, A. L.; Müssnich, L. A.; Manhabosco, T. M.; Chacham, H.; Batista, R. J.; de Oliveira, A. B. *Nanotechnology* **2015**, *26*, No. 045707.
(50) Batista, R. J. C.; Ordejón, P.; Chacham, H.; Artacho, E. *Phys. Rev. B* **2007**, *75*, No. 041402.

DOI: 10.1021/acsomega.7b00061
ACS Omega 2017, 2, 1696−1701